Solid Earth Discuss., https://doi.org/10.5194/se-2018-14
Manuscript under review for journal Solid Earth
Discussion started: 21 March 2018
© Author(s) 2018. CC BY 4.0 License.

Solid Earth Discussions
Open Access
EGU

The influence of subducting slab advance and erosion on overriding plate deformation in orogen syntaxes

Matthias Nettesheim[1], Todd A. Ehlers[1], David M. Whipp[2], and Alexander Koptev[1]

[1]Department of Geology, University of Tuebingen, Tuebingen, Germany
[2]Department of Geosciences and Geography, University of Helsinki, Helsinki, Finland

Correspondence: Todd A. Ehlers (todd.ehlers@uni-tuebingen.de)

Abstract. Focused, rapid exhumation of rocks is observed at some plate corners, but the driving mechanisms remain poorly understood and contested. In this study, we use a fully coupled thermo-mechanical numerical model to investigate the effect of slab advance and different erosion scenarios on overriding plate deformation. The subducting slab in the model is curved in 3D, analogous to the indenter geometry observed in seismic studies. We find that the amount of slab advance dramatically changes the orientation of major shear zones in the upper plate and the location of rock uplift zones. Shear along the subduction interface facilitates the formation of a basal detachment situated above the indenter, causing localized rock uplift there. Switching from flat (total erosion) to more realistic fluvial erosion leads to variation of rock uplift on the catchment-scale. Here, deepest exhumation again occurred above the indenter apex. We conclude that the change in orientation and dip angle set by the indenter geometry facilitates creation of localized uplift regions as long as subduction of the down-going plate is active. Tectonic uplift is modulated on even smaller scales by lithostatic pressure from the overburden of the growing orogen, and highest rock uplift can occur when a strong tectonic uplift field spatially coincides with large erosion potential. This implies that both the geometry of the subducting plate and the geomorphic and climatic conditions are important for the creation of focused, rapid exhumation.

1 Introduction

Plate corners connect long curved plate boundary segments (Figure 1) in subduction settings observed around the world. The deformation around plate plate corners, also referred to as orogen syntaxes, has been the subject of widespread attention over the last years due to the high, sustained, and spatially focused exhumation with rates in excess of $5\,\mathrm{mm\,a^{-1}}$ over million-year timescales. Classic examples of focused rapid exhumation at syntaxes have been documented for the Namche Barwa (e.g. Burg et al., 1998; Enkelmann et al., 2011; Stewart et al., 2008) and Nanga Parbat (Craw et al., 1994; Crowley et al., 2009) Himalayan Syntaxes, as well as for the Saint Elias Syntaxis (Berger et al., 2008; Enkelmann et al., 2010; Falkowski et al., 2014) in Alaska. Despite nearly two decades of work, the tectonic- and climate-driven erosional mechanisms responsible for patterns and rates of upper plate deformation in these areas remain debated (Bendick and Ehlers, 2014; Lang et al., 2016; Wang et al., 2014; Zeitler et al., 2001). Plate corners are characterized by a unique 3D geometry of the subducting plate. The bending required by subduction on a sphere results in formation of long, slightly concave subduction segments connected by strongly bent, convex

Solid Earth Discuss., https://doi.org/10.5194/se-2018-14
Manuscript under review for journal Solid Earth
Discussion started: 21 March 2018
© Author(s) 2018. CC BY 4.0 License.

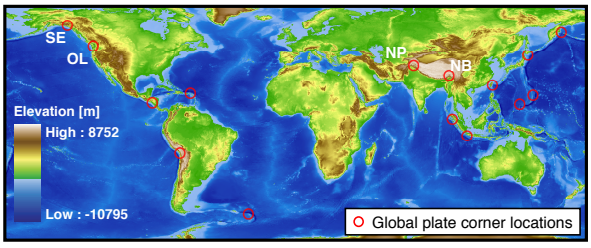

Figure 1. World map of plate corners. In these regions (red circles), changes in subduction orientation cause flexural buckling of the down-going plate (Mahadevan et al., 2010). These plate corner span a large variety of geodynamical and climatic settings and provide test cases to identify relevant mechanisms for rapid and focused exhumation.

arcs, the plate corners. These are flexurally stiffened by the bending and associated with the formation of orogen syntaxes (Mahadevan et al., 2010). This specific 3D shape can be clearly observed in seismic data from subduction zones, for example at the Cascadia subduction zone or the Alaskan plate corner (Hayes et al., 2012).

In many convergent plate settings, shortening is mostly accommodated by subduction of the down-going plate. However, an additional component of shortening can be taken up by slab advance, i.e. migration of the overriding plate toward the down-going plate (Heuret and Lallemand, 2005). The Nazca–South America subduction zone (Russo and Silver, 1994; Schellart et al., 2007), and the early stages of the India–Eurasia collision (Capitanio et al., 2010), provide examples of shortening with large amounts of slab advance. In previous studies, numerical modeling has played a central role towards understanding focused exhumation in orogen syntaxes. Work by Koons et al. (2002, 2013) simulated focused exhumation in syntaxes as a function of focused (climate driven) denudation. In their approach, they approximate the subsurface to be of homogeneous composition and define a straight S-line boundary between the subducting and the overriding plate, thus not accounting for the 3D geometry of subducting plates observed in many syntaxes. Although the link between erosion and uplift through isostasy is well established (Molnar and England, 1990; Montgomery, 1994; Simpson, 2004), their hypothesis of additional positive feedback by thermal weakening of the crust, causing accelerated deformation beneath deeply incised valleys (see also Zeitler et al., 2001), is controversial. Following this, work by Bendick and Ehlers (2014) considered the effect of the 3D subducting plate geometry, but with simplified upper plate rheology and erosion. In both of these previous approaches the kinematic boundary conditions were fixed, and the effect of different slab advance scenarios not considered.

In this study, we complement previous work by investigating how slab advance and erosion impacts the pattern and rates of exhumation in a rheologically realistic upper plate and in a generalized plate corner setting featuring a 3D-shaped, flexurally stiffened down-going plate. Our first aim in this study is the characterization of upper-plate deformation in slab advance settings with a subducting 3D indenter geometry. Our second aim is to understand the effect of erosional efficiency on upper-plate deformation and exhumation by contrasting total erosion (i.e. a constant flat surface) with more realistic fluvial erosion.

Solid Earth Discuss., https://doi.org/10.5194/se-2018-14
Manuscript under review for journal Solid Earth
Discussion started: 21 March 2018
© Author(s) 2018. CC BY 4.0 License.

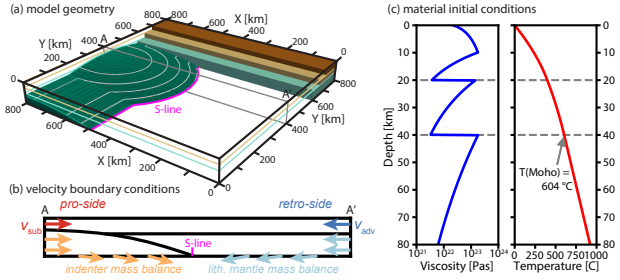

Figure 2. Model setup and properties. **a)** Cut-out oblique view of the model domain illustrating the geometry and material layers: The overriding plate is divided into an upper and lower crust and lithospheric mantle. The down-going plate is a uniform viscous material. **b)** Velocity boundary conditions. Downward rotation of the subducting plate and accretion at $x = 0\,\mathrm{km}$ with v_{sub}, as well as influx from $x = 800\,\mathrm{km}$ with v_{adv} is compensated up to the Moho depth by outflux at the bottom. **c)** Vertical profiles of the overriding plate effective viscosity and temperature initial conditions. Material parameters given in table 1.

2 Methods

2.1 Numerical model details

Geodynamical simulations of plate corner subduction zones are performed with the program DOUAR (Braun et al., 2008; Thieulot et al., 2008), a fully coupled three-dimensional thermomechanical numerical modeling program designed to solve visco-plastic creeping flow equations at the lithospheric scale. Models in DOUAR are defined by a set of velocity boundary conditions, material properties, and model geometry defining the material domains. Bulk velocities are the result of solving the quasi-steady state force balance equations for nearly incompressible fluids with a finite element approach on an octree mesh. Pressure values are derived indirectly from the velocity solution by the penalty method (e.g. Bathe, 1982) and local smoothing is applied to avoid small-scale pressure oscillations. Finally, temperature is computed, incorporating the effects of material velocities and thermal properties. Material interfaces and bulk volume properties are stored on a self-adapting cloud of particles advected within the model domain. Additional details of the model and governing equations are given in the appendix. For this study, we developed a new module that makes use of DOUAR's particle-in-cell approach and permits extraction of the pressure and temperature history (*p-T-t* paths) of particles exhumed at the free surface. Following the methods detailed in Braun (2003), Ehlers (2005), and Whipp et al. (2009), and using the parameters given therein, thermochronometric cooling ages can be calculated from these paths to quantify upper plate exhumation patterns and rates over time.

2.2 Model setup

2.2.1 Geometry

The model domain is $800\times800\,\mathrm{km}$ in planform and $81\,\mathrm{km}$ deep. The element size is $6.25\times6.25\times1.56\,\mathrm{km}$, corresponding to $128\times128\times52$ elements for the entire domain. The direction of subduction is parallel to the x axis and the entire setup is

Solid Earth Discuss., https://doi.org/10.5194/se-2018-14
Manuscript under review for journal Solid Earth
Discussion started: 21 March 2018
© Author(s) 2018. CC BY 4.0 License.

symmetric with respect to the $y = 400\,\mathrm{km}$ plane. Therefore, we refer to the $x = 0\,\mathrm{km}$ and $x = 800\,\mathrm{km}$ model boundaries as *left* and *right*, respectively, and to both $y = 0\,\mathrm{km}$ and $y = 800\,\mathrm{km}$ boundaries as model *sides*. The model consists of a layered overriding plate, which is divided into upper and lower crust and lithospheric mantle. The subducting plate on the left has a central bulge, referred to here as the indenter, and is $50\,\mathrm{km}$ high, $350\,\mathrm{km}$ wide and $400\,\mathrm{km}$ along dip. In contrast, the sides of the subducting plate are only $30\,\mathrm{km}$ high and terminate at $x = 320\,\mathrm{km}$ (see Fig. 2).

We simplify the model setup to approximate the effect of a flexurally stiffened indenter by prescribing the shape of the indenter and subducting plate shape as fixed through time. This approach minimizes internal deformation of the lower plate and ensures mass balance of the ingoing and outgoing subducted plate. This is achieved by assuming the shape and motion of the down-going plate to be rotational. The curved indenter and along-strike continuation of the plate referred to as the "background slab" are spheroidal and cylindrical in cross-section, respectively (Fig. 2).

Additionally, a thin, weak layer on top of the down-going plate is added to ensure partial decoupling, which also reduces indenter deformation (cf. Willingshofer and Sokoutis, 2009). The thickness of this weak layer is varied along strike in order to compensate for the changing depth to the slab, such that material inflow along the left domain edge is well-nigh horizontal.

2.2.2 Material parameters

Corresponding to the focus of this study, we use different material properties for the down-going and the overriding plate. In order to approximate the flexural stiffening of the buckled slab, we use a constant viscosity of $10^{25}\,\mathrm{Pa\,s}$ and no plasticity for the rigid subducting plate. For the overriding plate, we adopt a layered, visco-plastic rheology. The ductile properties of the upper crust, lower crust, and lithospheric mantle are based on wet granite, dry diabase, and olivine viscous flow laws, respectively (Carter and Tsenn, 1987; Hirth and Kohlstedt, 2003; Jadamec and Billen, 2012). The lithospheric mantle viscosity was designed to conform to the known deformation of olivine aggregates (Hirth and Kohlstedt, 2003). Its pressure dependence was eliminated by using parameters from Jadamec and Billen (2012) and recalculation of the remaining parameters (i.e. stress exponent and activation energy) under lithostatic pressure conditions. Brittle parameters are uniform in the crust with a $10\,\mathrm{MPa}$ cohesion and an initial friction angle of 15°. Strain softening reduces the friction angle to 5° at a strain value of 0.55. In the lithospheric mantle, the friction angle is constant 10°. All material parameters are summarized in table 1.

2.2.3 Temperature setup

Model temperatures are set by constant temperature boundary conditions of $0°\mathrm{C}$ at the surface and $930°\mathrm{C}$ at the bottom. Heat production in the upper and lower crust is chosen to reproduce the thermal structure of Bendick and Ehlers (2014). At startup, temperatures are run to conductive steady state, resulting in a Moho temperature of $604°\mathrm{C}$ and heat flux of $24\,\mathrm{mW\,m^{-2}}$ and $68\,\mathrm{mW\,m^{-2}}$ at the model bottom and surface, respectively. Since the indenter viscosity is temperature-independent, this temperature setup can be applied to the entire model domain.

Solid Earth Discuss., https://doi.org/10.5194/se-2018-14
Manuscript under review for journal Solid Earth
Discussion started: 21 March 2018
© Author(s) 2018. CC BY 4.0 License.

	Upper Crust Wet Granite[a]	Lower Crust Dry Diabase[a]	Lithospheric Mantle Olivine aggregates[b]
Density ρ [$\mathrm{kg\,m^{-3}}$]	2750	2900	3300
Thermal Diffusivity $k/\rho c$ [$10^{-6}\,\mathrm{m^2\,a^{-1}}$]	1.0	1.0	1.0
Heat Production [$\mu\mathrm{W\,ka^{-1}\,m^{-3}}$]	1.8	0.6	0.0
Viscosity Prefactor B [$\mathrm{Pa\,s^{1/n}}$]	$4.43{\cdot}10^7$	$1.24{\cdot}10^6$	$1.21{\cdot}10^7$
Activation Energy Q [$\mathrm{kJ\,mol^{-1}}$]	140.6	276.0	324.3
Stress Exponent n [1]	1.9	3.05	3.5
Cohesion C_0 [MPa]	10	10	2
Friction Angle ϕ [°]	$15 \rightarrow 5$	$15 \rightarrow 5$	10
Strain Weakening Interval [1]	$0.05 \rightarrow 0.55$	$0.05 \rightarrow 0.55$	-

a Carter and Tsenn (1987)

b Hirth and Kohlstedt (2003); Jadamec and Billen (2012)

Table 1. Overriding pate material parameters

2.2.4 Boundary conditions

In the first part of this study, we investigate the effect of different slab advance scenarios. In the case of *no slab advance*, all shortening is taken up by subduction and accretion, i.e. material inflow into the domain only from left side ($v_{\mathrm{sub}} = 30\,\mathrm{mm\,a^{-1}}$, $v_{\mathrm{adv}} = 0$). *Full slab advance* corresponds to inflow only from the right side ($v_{\mathrm{sub}} = 0,\ v_{\mathrm{adv}} = 30\,\mathrm{mm\,a^{-1}}$) and in the case of *half advance* both velocities are equal ($v_{\mathrm{sub}} = v_{\mathrm{adv}} = 15\,\mathrm{mm\,a^{-1}}$). This means the S-line, intersection of overriding and down-going plate at the bottom boundary of the model domain (see Figure 2), is kept at a constant position. To allow better comparison between model scenarios, the overall shortening rate $v_{\mathrm{short}} = v_{\mathrm{adv}} + v_{\mathrm{sub}}$ is kept constant at $30\,\mathrm{mm\,a^{-1}}$, so that the model mass balance is the same for all cases. Additionally, outflux at the bottom of the lithospheric mantle increases from zero at the right boundary toward the center in order to compensate material influx from the right. This ensures all ratios of v_{sub} and v_{adv} effect the same mass added to the model domain.

2.2.5 Erosion

The second part of this study contrasts two erosion scenarios of flat and fluvial erosion. Flat (or total) erosion removes all material uplifted above the initial surface elevation instantly. In this special case, rock uplift rate is equal to the exhumation rate (England and Molnar, 1990). For more realistic fluvial and diffusive erosion the landscape evolution model *FastScape* (Braun and Willett, 2013) was coupled to DOUAR.

Fluvial erosion is computed on a regular grid of $0.78\,\mathrm{km}$ resolution with uniform precipitation of $1\,\mathrm{mm\,a^{-1}}$. Erosion constants were $8.0{\cdot}10^{-5}\,\mathrm{m^{-2}}$ for fluvial and $4.0\,\mathrm{m^2\,a^{-1}}$ for hillslope erosion with a stream power exponent of 0.4. The edges at

Solid Earth Discuss., https://doi.org/10.5194/se-2018-14
Manuscript under review for journal Solid Earth
Discussion started: 21 March 2018
© Author(s) 2018. CC BY 4.0 License.

Table 2. Controlling Parameters Overview

Model name	v_{sub}	v_{sub}	Erosion type
No advance	100 %	0 %	flat
Half advance	50 %	50 %	flat
Full advance	0 %	100 %	flat
Fluvial erosion	50 %	50 %	FastScape

$x = 0\,\text{km}$ and $x = 800\,\text{km}$ are fixed to baselevel and local minima are filled so that each catchment drains to one of those edges.

2.2.6 Thermochronometric cooling ages

Thermochronometric cooling ages are calculated using tracer particles within the domain, and assuming no deformation for 30 Myr prior to the model start. Each predicted age represents an integration of deformation from its respective partial annealing or retention zone to the surface (Dodson, 1973; Reiners et al., 2005). Consequently, exhumation of material from the respective zone to the surface is required before the predicted cooling age can be interpreted in a meaningful way. As thermochronometric ages are sensitive to both changes in particle trajectory and thermal gradients, thermochronometric ages will continue to adjust to the evolving geodynamic conditions after the initial phase.

3 Results

We investigate the effects of crustal shortening by both subduction and frontal accretion ($v_{\text{sub}} > 0$) and slab advance ($v_{\text{adv}} > 0$) on upper crust deformation in a subduction zone with a rigid indenter in the central part of the model domain. We evaluate those models with respect to the resulting rock uplift and strain rates due to the variation in boundary inflow velocities. Additionally, we discuss the models' temporal evolution and the predicted thermochronometric ages. In total, we present four models. The first three (no, half, and full advance) are run with flat erosion, the fourth (fluvial erosion) uses the half advance velocity boundary conditions with fluvial instead of flat erosion. An overview is presented in table 2.

3.1 Effect of slab advance on strain rate distribution

Figure 3 illustrates the key features of the half advance model in a snapshot taken after 4 Myr modeling time. Strain rates (background colors in panel a) indicate two main systems of localized deformation (strain rates above $5.0{\cdot}10^{-15}\,\text{a}^{-1}$). In the first system, two broad, steeply dipping shear bands rooting to the S-line at an angle of $\sim 60°$ form a lithospheric scale pop-up structure. Due to the mostly viscous deformation (cf. Fig. 2), the shear bands are poorly localized in the lower crust and lithospheric mantle. Laterally towards the model center and the indenter ($y = 400\,\text{km}$), those shear bands attenuate. Here, deformation is accommodated by the second type of structure, a basal detachment located above the indenter. The particle

Solid Earth Discuss., https://doi.org/10.5194/se-2018-14
Manuscript under review for journal Solid Earth
Discussion started: 21 March 2018
© Author(s) 2018. CC BY 4.0 License.

trajectories shown on the slices at $y = 50$, $225\,\mathrm{km}$ show that material is transported horizontally towards the S-line, where paths for crustal material turn upward and the lithospheric mantle is gradually subducted. The temperatures shown in panel b) indicate two anomalies that correspond with the two major shear zones. Towards the model sides, temperatures undulate following the bent Moho. Likewise, temperatures above the indenter apex are elevated at the location of the basal detachment.

Different amounts of slab advance change the distribution of strain rates significantly, as can be seen from Figure 4. In the no slab advance (Fig. 4a), the structures to the left of the S-line, the pro-shear band and the basal detachment, are expressed even more strongly than in the half advancing scenario, whereas the retro-shear band is weaker. The case of full slab advance (Fig. 4b) exhibits the opposite behavior: The retro-shear zone to the right of the S-line is more active, while the structures on the left are expressed more weakly. In both end-member cases, a shallow basal detachment forms in the upper crust above the more active of the steeply dipping shear bands, which is not observed in the half advance case.

3.2 Effect of slab advance on the spatial distribution of rock uplift

Figure 5 shows two horizontal slices of the rock uplift rate at the surface and $10\,\mathrm{km}$ depth for the three scenarios. In general, three zones of rock uplift, corresponding to the detachments described in the previous section, can be identified. Two bands of uplift to the right and left of the S-line, associated to the steeply dipping pro- and retro-shear zones, respectively, and a curved ellipsis located above the indenter basal detachment. In all scenarios, the mean uplift rate is about $1.3\,\mathrm{mm\,a^{-1}}$, but the distribution strongly depends on slab advance velocity. For no slab advance ($v_{\mathrm{sub}} = 100\,\%$, $v_{\mathrm{adv}} = 0\,\%$), the pro-side shear zones, i.e. those above the background slab and the indenter ellipsis, show the highest rock uplift rates (6.4 and $8.3\,\mathrm{mm\,a^{-1}}$), respectively). In the half advance scenario ($v_{\mathrm{sub}} = 50\,\%$, $v_{\mathrm{adv}} = 0\,\%$), rock uplift is concentrated mostly in the indenter ellipsis ($8.0\,\mathrm{mm\,a^{-1}}$). Finally, the full advance scenario ($v_{\mathrm{sub}} = 0\,\%$, $v_{\mathrm{adv}} = 100\,\%$) exhibits only a comparatively small increase of rock uplift above the indenter ($5.4\,\mathrm{mm\,a^{-1}}$), whereas the right-side uplift band is well pronounced with rates reaching $6.3\,\mathrm{mm\,a^{-1}}$. For all scenarios, the horizontal distribution of rock uplift rates at $10\,\mathrm{km}$ depth mimics the pattern at the surface, but uplift rates are attenuated by roughly $50\,\%$, indicating that upward motion is concentrated at shallow depths.

3.3 Relative slab motion effects on temporal evolution

As simulation time progresses, the deformation patterns and rock uplift change differently for the three scenarios. The central region depicted in Figure 6 shows that both for the no and half advancing slab scenario, the uplift peak above the indenter increases and reaches a quasi-steady state. In case of full slab advance, it decreases after reaching a maximum at $\sim 4\,\mathrm{Myr}$. Here, the strong and lasting increase can be observed in the right uplift band instead. These changes in uplift are also reflected in the position and modes of shear zones (compare figs. 3 and 4 showing strain rates at $4\,\mathrm{Myr}$ modeling time with strain rates at $8\,\mathrm{Myr}$ in Fig. 6). Without slab advance, the indenter basal detachment slowly shifts to the right over time, while keeping its general shape. In contrast, additional shear zones develop alongside the basal detachment for the half advance scenario. In the case of full slab advance, however, motion across the basal detachment almost ceases in favor of a newly formed normal fault.

Solid Earth Discuss., https://doi.org/10.5194/se-2018-14
Manuscript under review for journal Solid Earth
Discussion started: 21 March 2018
© Author(s) 2018. CC BY 4.0 License.

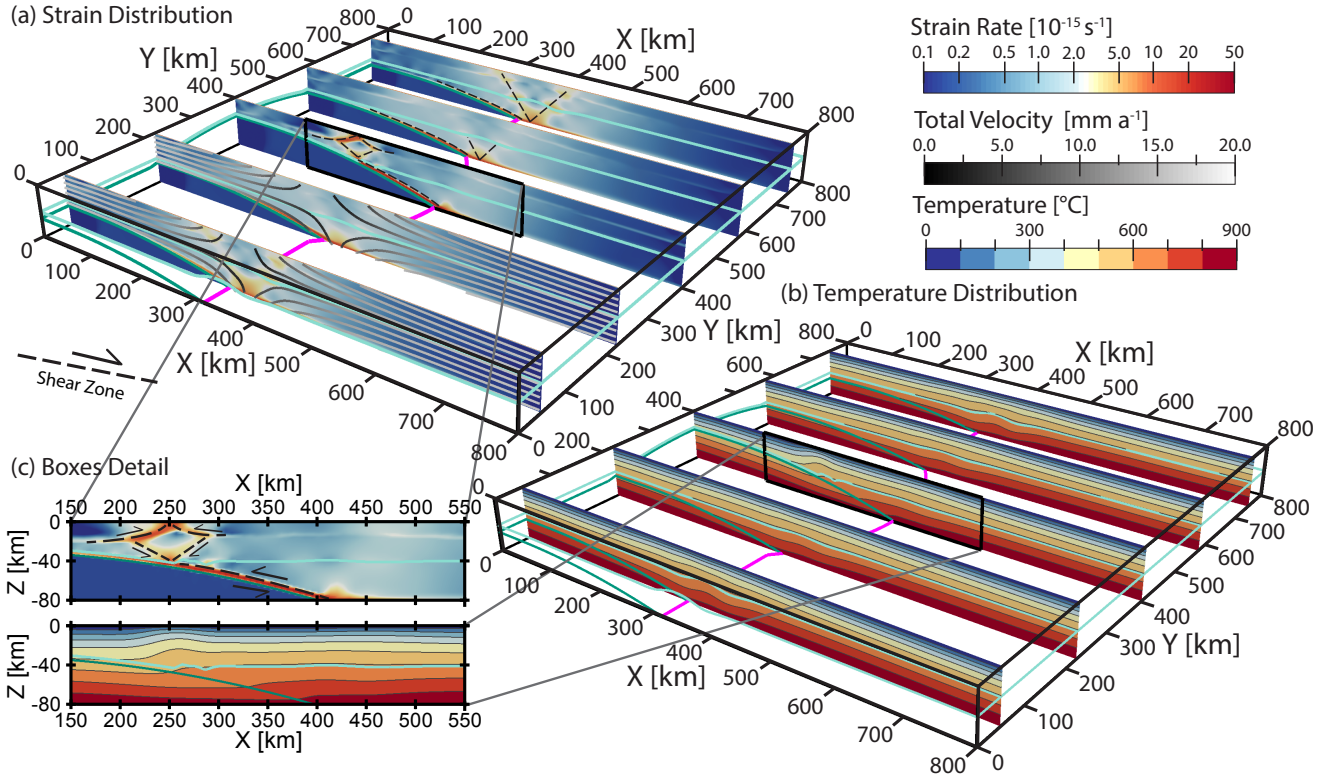

Figure 3. Vertical slices along dip after 4.0 Myr modeling time showing the second invariant of the strain rate tensor, particle trajectories, and the temperature distribution for the half advance scenario. Outlines of the Moho (light green), subducting plate interface (dark green), and S-line (magenta) are added for orientation. Note that results and slices are symmetrical about the $y = 400$ km plane. **a)** The strain rate outlines the major shear zones: Two broad, poorly localized shear zones nucleate at the S-line, while the pro-shear zone weakens towards the model center. This shear is accommodated by a basal detachment that is situated on top of the indenter. **b)** Temperatures follow crustal deformation. Significant upward heat advection can be seen in the vicinity of the basal detachment, while Moho deformation dominates the temperature anomalies towards the model sides.

3.4 Prediction of thermochronometric ages

Figure 7 shows thermochronometric age predictions and physical parameters of exhumed material for the half advancing slab after 8 Myr modeling time and illustrate the possibilities of the newly added particle tracing module. The relative distribution of predicted cooling ages is similar for all systems and the relative increase in age corresponds to the respective increase in closure temperature. Likewise, all physical parameters show the same pattern, which resembles that of rock uplift rates at the surface (cf. Fig. 5). Although of similar range, cooling ages above the indenter are systematically younger in the area above the indenter compared to those from the uplift band at the model sides.

Solid Earth Discuss., https://doi.org/10.5194/se-2018-14
Manuscript under review for journal Solid Earth
Discussion started: 21 March 2018
© Author(s) 2018. CC BY 4.0 License.

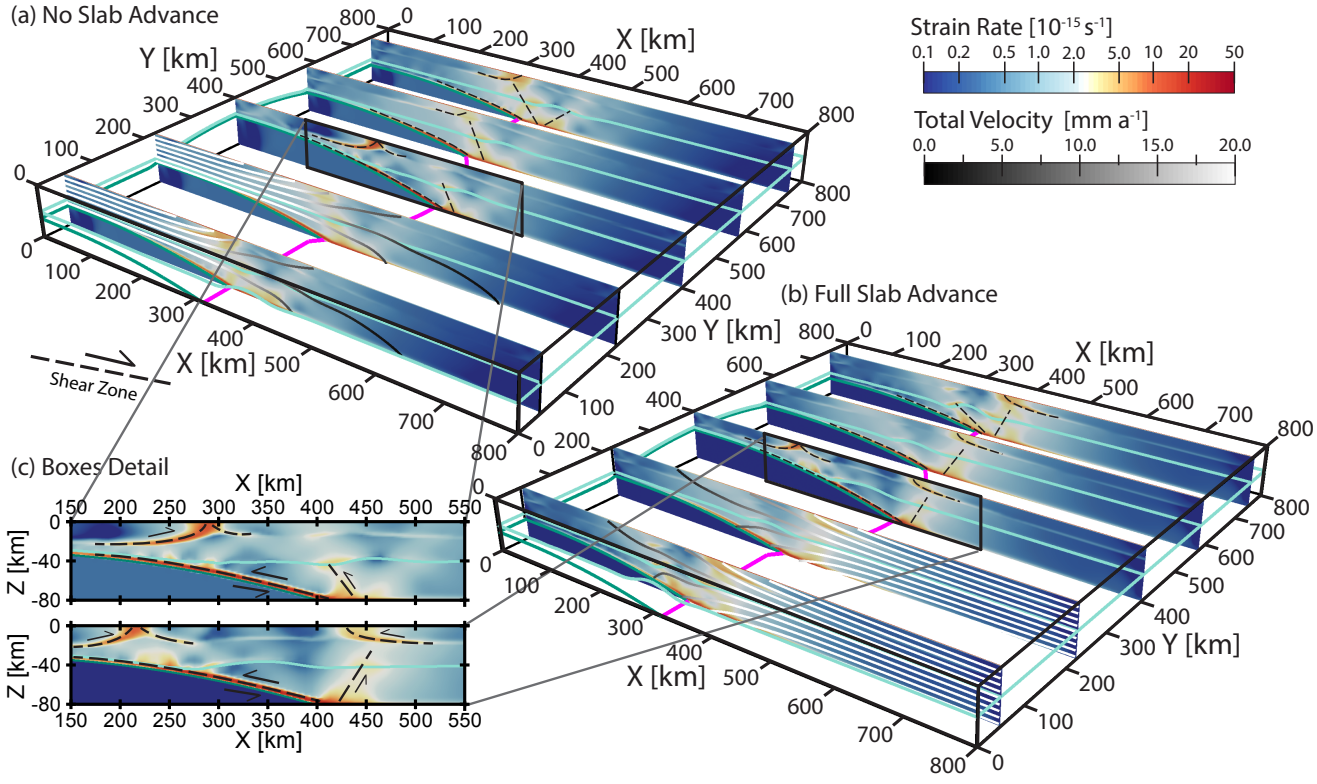

Figure 4. Vertical slices after 4.0 Myr modeling time showing the second invariant of the strain rate tensor and particle trajectories for **a)** no and **b)** full slab advance scenarios. Outlines of the Moho (light green), subducting plate interface (dark green), and S-line (magenta) are added for orientation. The main shear zone rooting to the S-line is oriented towards the direction of influx. At shallow depths, that shear zone forms a basal detachment in the respective orientation. The basal detachment above the indenter exists for both cases, but is pronounced more strongly in the no slab advance scenario.

Figure 8 shows a comparison of resulting zircon (U–Th)/He cooling ages and rock uplift rates for the three flat erosion scenarios. In all cases, the distribution of cooling ages again matches that of rock uplift rates. The shift in deformation towards the direction of inflow is clearly visible. Additionally, the concentration of young ages above the indenter can be seen in all scenarios. Even in the case of a fully advancing slab (Fig. 8c), where most deformation is accommodated by the right steeply dipping shear zone, this increase towards the center is visible in the zircon (U–Th)/He ages.

3.5 Effect of variable erosion on exhumation

For the half advance velocity boundary conditions, an additional simulation coupled to a landscape evolution model (*FastScape*, Braun and Willett (2013)) was performed. The distribution of strain rates and large-scale particle trajectories, as described in

Solid Earth Discuss., https://doi.org/10.5194/se-2018-14
Manuscript under review for journal Solid Earth
Discussion started: 21 March 2018
© Author(s) 2018. CC BY 4.0 License.

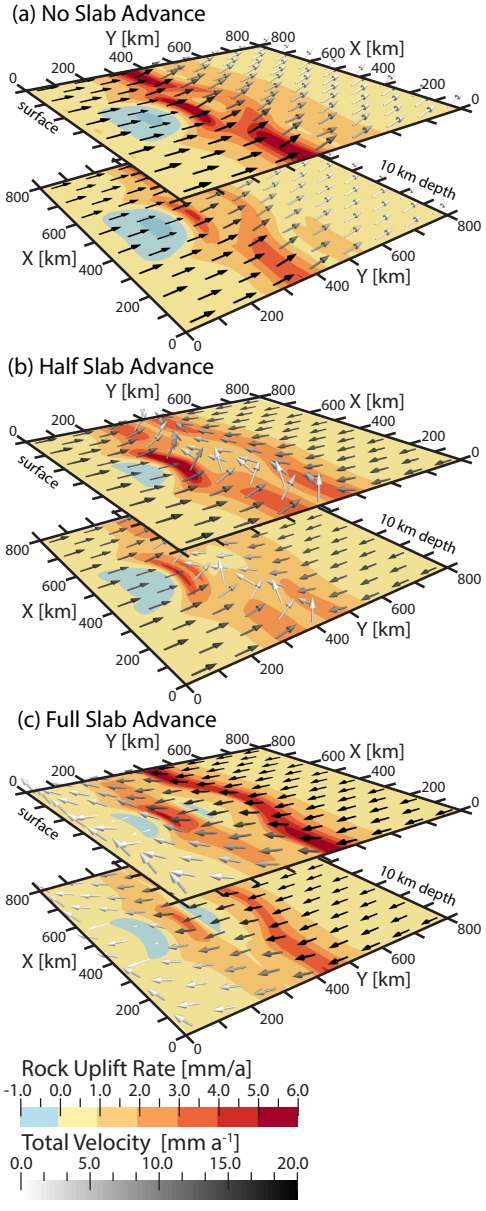

Figure 5. Rock velocity field and uplift rates after 2.5 Myr modeling time. Each panel shows two horizontal slices at the surface and 10 km depth for the three scenarios discussed, i.e. **a)** no, **b)** half, and **c)** full advancing slab. Background colors show rock uplift rate, with red tones indicating uplift and blues subsidence. Arrows illustrate the full 3-dimensional velocity field and are colored by total velocity. Rock uplift occurs in two bands along the S-line and in an ellipsoid region above the indenter. The relative uplift rate in the two bands depends on the inflow velocity ratio. For both no and half advancing slab, uplift above the indenter is equally strong, but more distinguished in the half advancing scenario.

Solid Earth Discuss., https://doi.org/10.5194/se-2018-14
Manuscript under review for journal Solid Earth
Discussion started: 21 March 2018
© Author(s) 2018. CC BY 4.0 License.

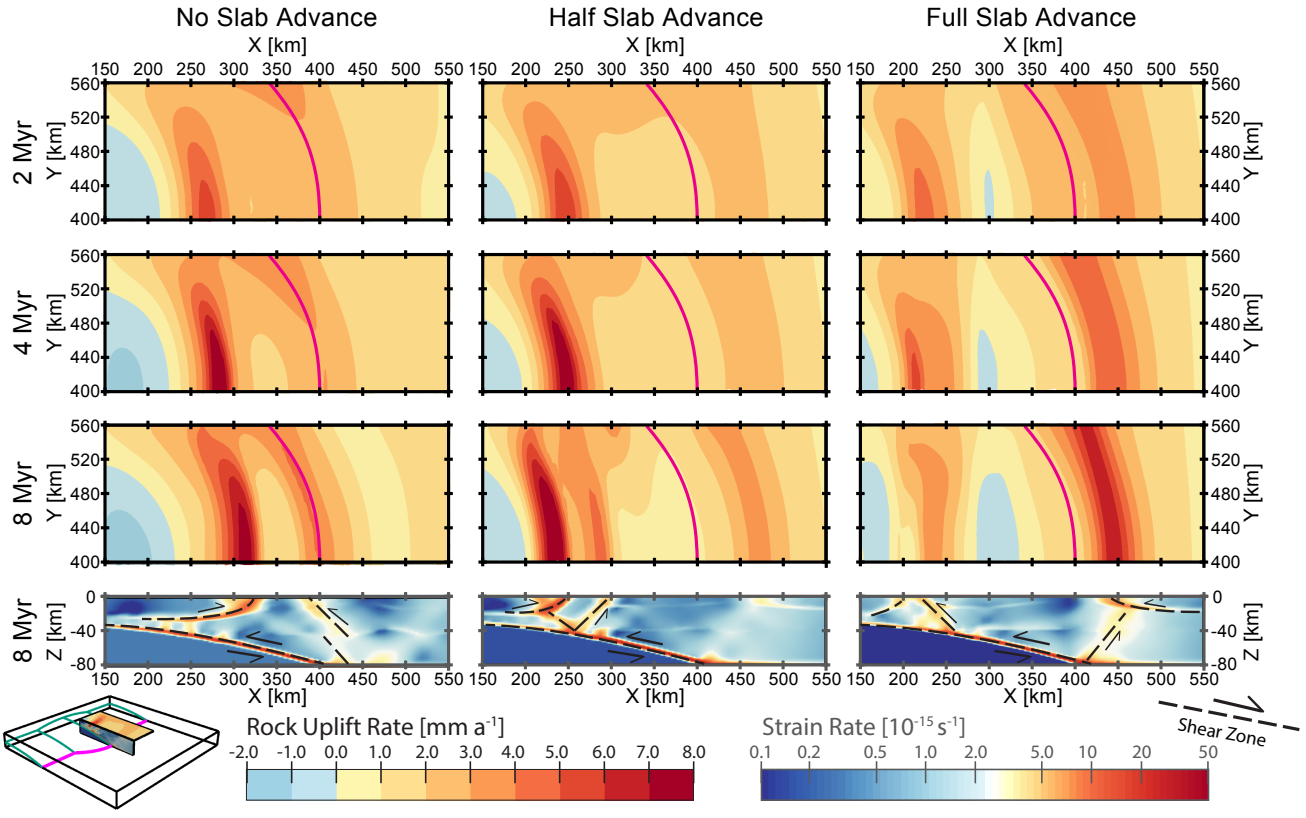

Figure 6. Rock uplift rates for the no, half, and fully advancing slab scenarios at 2, 4, and 8 Myr modeling time, and strain rates on the $y = 400$ km cross-section at 8 Myr. The panels are cropped to the region of interest of $x = 150$–550 km and $y = 400$–560 km. No advance slab scenario shows a basal detachment in dynamic steady state that slowly migrates to the right. In the half advancing scenario, uplift above the indenter likewise reaches a plateau, but its position is stable and additional shear zones form in the last stage. Lastly, the full advance case exhibits most uplift at the right uplift band, which continuously increases, whereas the indenter uplift ceases again after reaching a peak at 4 Myr modeling time.

section 3.1, are only weakly affected by this switch to fluvial erosion. However, the creation of topography and the resulting variations in lithostatic pressure cause changes in upper crustal deformation as illustrated by Figure 9.

Panel a shows the topography created after 6.0 Myr modeling time, with highest peaks towards the model edge and lower topography and a curved flank above the indenter. The distribution of rock uplift shown in panel b forms two broad bands situated on the flanks of the forming orogen. The left band follows the shape of the slab contour at 50 km depth, with a slight increase in uplift rate above the indenter apex, the right one is only slightly curved and located at $x = 500$ km. In comparison with flat erosion (shown in panel d), rock uplift zones are much wider, especially towards the model sides, and uplift rates are reduced by roughly half. Additionally, there are strong local variations, with peaks in rock uplift situated in river valleys. These

Solid Earth Discuss., https://doi.org/10.5194/se-2018-14
Manuscript under review for journal Solid Earth
Discussion started: 21 March 2018
© Author(s) 2018. CC BY 4.0 License.

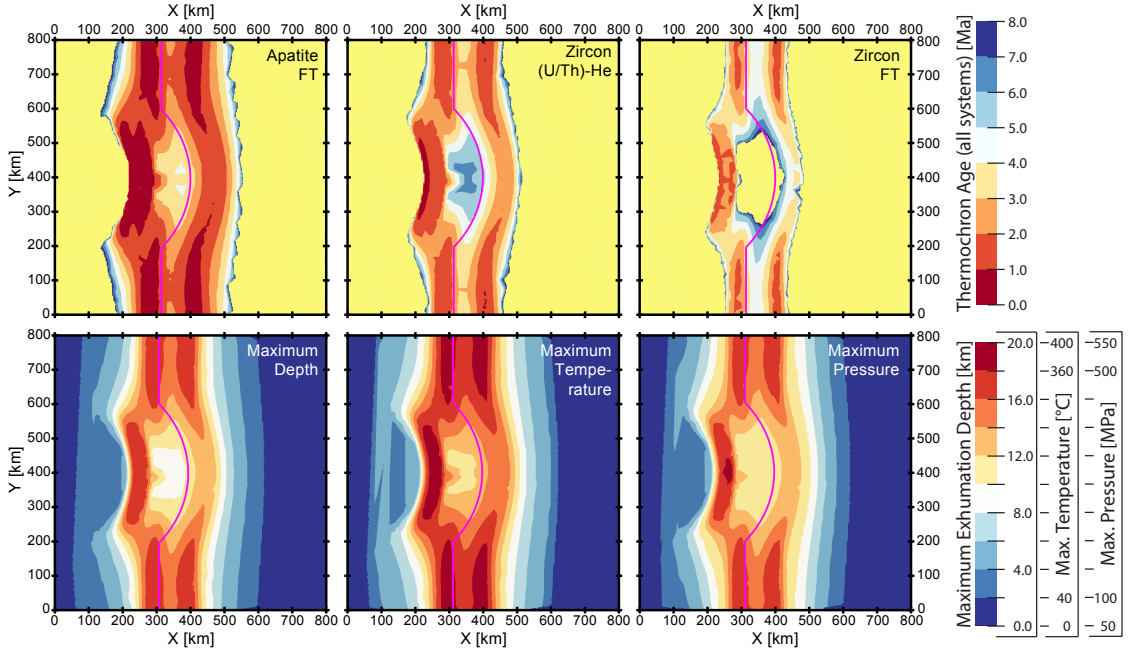

Figure 7. Thermochronometric cooling ages (apatite fission track, zircon (U–Th)/He, and zircon fission track) and physical exhumation parameters (maximum depth, temperature, and pressure) after 8 Myr simulation time. All observables clearly follow the pattern set by rock uplift rates of two bands at the model edge and a localized region of uplift above the indenter. Thermochronometric age is increasingly older with a higher closing temperature of the respective system.

local maxima (up to 2.9 $\mathrm{mm\,a^{-1}}$ compared to an average 1.0 $\mathrm{mm\,a^{-1}}$) correspondingly show deeper exhumation, as can be seen from panel c. The two uplift peaks in the marked catchments show the deepest exhumation ($\sim$8 km). They are situated above the indenter and within the region of deepest exhumation in the flat erosion scenario, shown in panel e for comparison. They also comprise locations where the youngest thermochronometric ages are predicted (not shown). In summary, fluvial erosion leads to variation of rock uplift and exhumation on the catchment scale and maxima in rock uplift roughly 60 km in diameter, while regions of high uplift in the flat erosion scenarios extend $\sim$250 km along strike. These zones of deepest and fastest exhumation are situated above the indenter apex.

4 Discussion

4.1 Summary of model results and indenter geometry effect

In all flat erosion scenarios, shortening is accommodated by a lithospheric-scale pop-up structure comprising two shear bands that root to the S-line along the background slab. They give rise to two bands of uplift that follow the S-line trace, while

Solid Earth Discuss., https://doi.org/10.5194/se-2018-14
Manuscript under review for journal Solid Earth
Discussion started: 21 March 2018
© Author(s) 2018. CC BY 4.0 License.

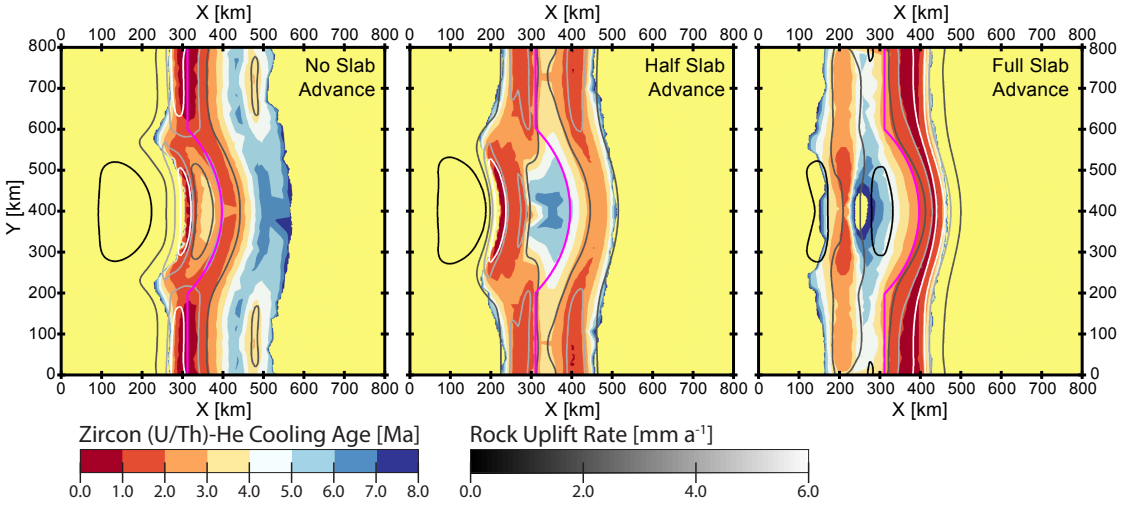

Figure 8. Comparison of zircon-(U–Th)/He cooling age for three slab advance scenarios. In all cases, cooling ages match well with the distribution of rock uplift. The shift in deformation focus in direction of the main material influx is clearly visible.

the pro-band diminishes towards the model center. There, above the indenter apex, a basal detachment formes and creates a spatially focused region of uplift.

The two main factors for the differences between the indenter and background sections of the subducting slab can be attributed to the slab geometry. The shallower slab and lower dip angle of the indenter exerts a stronger traction on the overriding plate, both forward and downward, that furthers the development of the observed basal detachments. Additionally, the steeper dip of the indenter at depth provides better conditions for strain transfer along the interface than the background slab, so that no additional shear zone is needed to accommodate shortening in this region. It important to note that the different depths to the subducting slab may contribute to those effects. Nevertheless, the variation of slab dip angles conforms to natural conditions. A prime example are the Olympic mountains, where the accretionary wedge is exposed on land only above the observed slab bulge (Brandon et al., 1998), which illustrates the substantial effects changes in the subducting slab geometry can cause.

4.2 Effect of slab advance on strain rates

The slab advance velocity has a first-order influence on the orogen dynamics, as the steeply dipping shear zone oriented toward the primary influx direction is expressed more strongly. Contrary to two other scenarios, the basal detachment in the full advance case is only of transient nature (cf. Fig. 6), and rock uplift rates above this feature reach barely half those seen in the other scenarios. As much of the overall shortening in this case is taken up by the retro-shear band, even increasing by time through thermal and strain weakening, strain transfer along the weak subduction interface and thus uplift on this side is strongly reduced.

Solid Earth Discuss., https://doi.org/10.5194/se-2018-14
Manuscript under review for journal Solid Earth
Discussion started: 21 March 2018
© Author(s) 2018. CC BY 4.0 License.

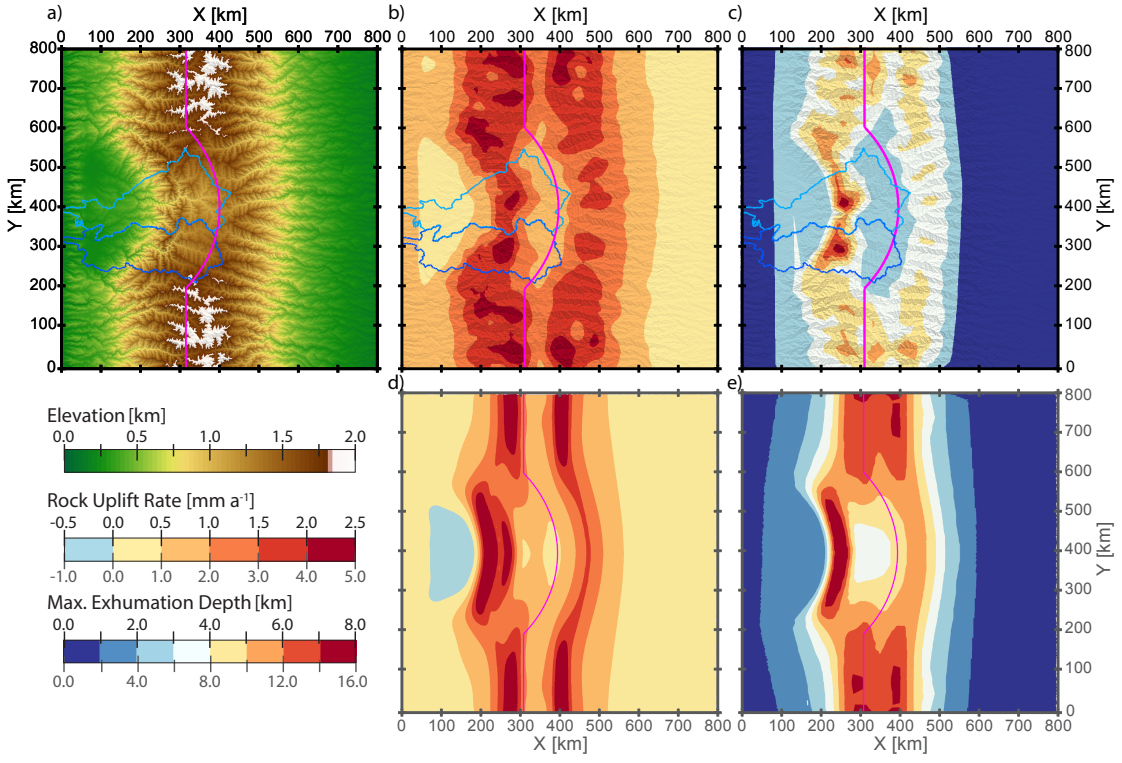

Figure 9. Comparison of rock uplift and exhumation depths with fluvial versus total erosion. **a)** Surface elevations, **b)** rock uplift rates, and **c)** exhumation depth for the half advance scenario coupled to a landscape evolution model (*FastScape* (Braun and Willett, 2013)) after 6.0 Myr modeling time. Uplift is focused along the flanks of the orogen, with exhumation maxima situated in river valleys of high erosion potential. Deepest exhumation occurs in the two uplift foci situated above the indenter, the catchments outlined in blue. Predicted thermochronometric ages are: apatite (U–Th)/He: 1.3 and 1.1 Ma; apatite fission track: 1.9 and 1.65 Ma; and zircon (U–Th)/He 4.2 and 4.1 Ma for the upper (light blue catchment) and lower (dark blue) hotspot respectively. **d)** and **e)** show the flat erosion results for rock uplift rates and exhumation depth for comparison. Note the range is increased by factor 2 for those two plots (gray labels).

The half and no advance scenarios, however, reach a dynamic steady state at ∼4 Myr. Due to no opposing influx, the peak position in the no slab advance scenario continues to move 50 km forward in 8 Myr of modeling time, but the general structure of shear zones and strain distribution stays the same. The half advance scenario is the intermediate case and shows features of both other scenarios, with a stronger retro-shear zone and a persistent, but spatially stable, basal detachment above the indenter.

4.3 Effect of slab advance on exhumation and cooling ages

Exhumation and rock uplift, which are the same in case of flat erosion, are defined by the orogen-scale dynamics discussed in the previous section. Deformation and uplift are strongest in a broad region along the S-line, with a localized region of uplift created by the basal detachment, if active. The amount of slab advance influences rock uplift through the relative activity (or

Solid Earth Discuss., https://doi.org/10.5194/se-2018-14
Manuscript under review for journal Solid Earth
Discussion started: 21 March 2018
© Author(s) 2018. CC BY 4.0 License.

rate of deformation) of shear bands as discussed in the previous section. Higher slab advance velocities cause faster rock uplift along the right uplift band, whereas more frontal accretion strengthens the left band and centers the uplift above the indenter. In the no and half advance scenarios, rock uplift rates above the indenter reach 7.5 $\mathrm{mm\,a^{-1}}$ at 3.5-4 Myr, but only 4 $\mathrm{mm\,a^{-1}}$ in the fully advancing slab scenario, decreasing again after 4 Myr.

4.4 Sensitivity of exhumation to different erosion parameters

On large scales, the relative distribution of rock uplift is similar for both perfect and fluvial erosion model runs. Nevertheless, the growing topography produces an increased lithostatic overburden, causing both a general reduction in rate and spatial variations in rock uplift on the catchment scale. Higher uplift rates are situated in valleys, and the deepest and fastest exhumation is observed above the indenter apex, where strong tectonic forcing coincides with a high erosion potential, in this case through the large upstream catchment area.

From the previous results, we hypothesize that both focused deformation and focused erosion are necessary in order to form a region of localized and rapid uplift. The curved 3D-geometry of the subducting plate at plate corners sets the stage, as proposed by Bendick and Ehlers (2014) but only when this concurs with a sufficiently high erosion potential, a spatially limited area of intense uplift can form (cf. Zeitler et al., 2001).

A prime example for this are the Himalayan syntaxes, where the Yarlung and Ganges river, respectively, cut across the Himalayan range and steepen rapidly (Finlayson et al., 2002). In combination with active crustal-scale structures (Burg et al., 1998; Schneider et al., 1999), this has given rise to spatially limited, rapid exhumation as indicated by very young thermochronometric cooling ages (Zeitler et al., 1993; Winslow et al., 1996; Burg et al., 1998; Malloy, 2004; Zeitler et al., 2014)

4.5 Comparison to previous work

This work combines and builds upon previous work. Koons et al. (2002) showed that locally enhanced erosion rates and preweakened crust can lead to focused exhumation. However, they used a uniform visco-plastic material for both overriding and down-going plate and a straight S-line and material influx and basal drag only on one side, corresponding to our no advance scenario. Flat erosion was applied in only a limited region, while surrounding areas were not eroded, resulting in highest rock uplift rates in this very region. In contrast, Bendick and Ehlers (2014) used an indenter-type geometry, but temperature-dependent viscous rheology for the overriding plate and uniform, flat erosion. Due to the viscous rheology, no strain localization was observed and rock uplift rates increased gradually from the edges toward the center, forming an uplift region of several 100 km extent. While they explored effects of viscosity and indenter geometry, only full slab advance velocity boundary conditions were used.

The addition of frictional plasticity in this study naturally allows for strain localization. In combination with fluvial erosion, this illustrates possible mechanisms that create localized regions of uplift without relying on a priori defined structures.

Solid Earth Discuss., https://doi.org/10.5194/se-2018-14
Manuscript under review for journal Solid Earth
Discussion started: 21 March 2018
© Author(s) 2018. CC BY 4.0 License.

4.6 Model caveats and limitations

Our model setup is generic and includes first-order features of plate corner settings, but is not designed reproduce a specific region. Numeric resolution and large uncertainties on rheologic and thermal parameters do not permit this. Moreover, rock uplift rates in our model are overestimated for flat erosion simulations (section 3.1–4.3; figs. 3–6), which inhibits the creation of topography that would exert an isostatic counter-force to material uplift. With these caveats in mind, rock uplift rates in the flat erosion models should be seen as upper bound in cases of extremely high erosion. Corresponding to the high rock uplift rates, our predicted cooling ages are very young, but nevertheless consistent with the range of exhumation rates reported at syntaxes: $\sim$1 $\mathrm{mm\,a^{-1}}$ in the Olympic mountains (Brandon et al., 1998), 3–5 $\mathrm{mm\,a^{-1}}$ in SE Alaska St. Elias range (Enkelmann et al., 2016), and 5–9 $\mathrm{mm\,a^{-1}}$ in the eastern Himalayan syntaxis (Enkelmann et al., 2011; Lang et al., 2016).

It is also worth noting that in the fluvial erosion simulations, uniform precipitation was used throughout the model run. While this is justifiable for our study of contrasting erosional efficiency, it has been shown that changes in precipitation by orographic effects strongly influence the distribution of rock uplift and consequently orogen dynamics (Willett, 1999). If wind comes from the pro-side, the increased erosion might increase the focusing effect observed above the indenter apex, whereas we expect weaker erosion maxima with wind from the retro-side.

5 Summary and conclusion

In a generalized 3D curved slab subduction setting, the effect of velocity boundary conditions and erosion on the deformation in the overriding plate is investigated, with focus on the emergence and properties of localized rock uplift. Particle tracking and thermochronometric age prediction has been added to and existing model (DOUAR) to allow for direct and more tangible evaluation of crustal deformation.

The common point of all models is the localization of deformation in two major systems. One is an pop-up structure composed of two steeply dipping shear bands rooting to the S-line and cutting across the entire lithospheric mantle and crust. The shear bands are expressed more strongly towards the model sides and toward the primary direction of inflow. For the no slab advance scenario, the retro-side shear band almost disappears, and in the case of a fully advancing slab, the pro-side shear band is much weaker. The second major shear system is a basal detachment situated above the indenter apex. This detachment is strongly expressed only for a not or half advancing slab and gives rise to a zone of localized rock uplift that reaches a quasi-steady state with uplift rates of 7.5 $\mathrm{mm\,a^{-1}}$ at $\sim$4 Myr. In case of a fully advancing slab, uplift rates reach only 4 $\mathrm{mm\,a^{-1}}$ and decreases after a peak at 3.5 Myr, when larger amounts of shortening are accommodated by the retro-shear zone.

Applying a landscape evolution model and the consequent creation of topography causes rock uplift to vary on smaller (catchment-) scale than previously set by tectonics alone. Deepest and fastest exhumation occurs where tectonic forcing coincides with large erosion potential.

Solid Earth Discuss., https://doi.org/10.5194/se-2018-14
Manuscript under review for journal Solid Earth
Discussion started: 21 March 2018
© Author(s) 2018. CC BY 4.0 License.

Code and data availability. Model output is available upon request from T. Ehlers. The software DOUAR is currently not open source. Requests for use should be made to the main author, Jean Braun (currently at GFZ Potsdam).

Appendix A: Numerical model details

Lithospheric deformation and temperatures in this study are calculated with the program DOUAR (Braun et al., 2008; Thieulot et al., 2008), a fully coupled three-dimensional thermomechanical model. Further details can also be found in Braun and Yamato (2010) and Whipp et al. (2014).

DOUAR solves the three-dimensional Stokes (creeping) flow equations for incompressible fluids, constituted by conservation of momentum (Eq. A1) and conservation of mass (Eq. A2):

$$\nabla \cdot \mu \left(\nabla \boldsymbol{V} + \nabla \boldsymbol{V}^T \right) - \nabla P = \varrho g; \tag{A1}$$

$$\nabla \boldsymbol{V} = 0, \tag{A2}$$

where μ is the material shear viscosity, $\boldsymbol{V}$ is the velocity field, P the pressure, ϱ is the density and g gravity acceleration. The solution is computed with the finite element method using Q1P0 elements, i.e. the pressure is calculated from the velocity field by the penalty formulation (e.g. Bathe, 1982):

$$P = -\lambda \nabla \cdot \boldsymbol{V}. \tag{A3}$$

For this, conservation of mass is amended to near incompressibility with a penalty factor λ, which is typically eight orders of magnitude larger than the viscosity μ. The model domain is subdivided into elements by a regular grid, on which the finite element solution is calculated.

The material properties of each element are defined by marker particles of two types, that a) track material interfaces (*surfaces*) or b) record strain and pressure (*cloud*). Particles will be created or deleted automatically to ensure both a roughly homogeneous particle density and adequate base for material property calculations (*self-adapting density*). Additionally, a third type of particles stores position, temperature and pressure for each time step. If those particles are exhumed at the surface, the p-T-t path is compiled from storage and registered at the current time step. From these paths, thermochronometric cooling ages can be calculated.

Materials can be either purely viscous or frictional visco-plastic. The viscosity μ follows a thermally activated creep law:

$$\mu = \mu_0 \dot{\varepsilon}^{1/n-1} e^{Q/nRT} \tag{A4}$$

where μ_0 is the intrinsic viscosity, $\dot{\varepsilon}$ the second invariant of the deviatoric strain rate tensor, n the stress exponent, Q the activation energy, R the gas constant and T the temperature. If the stress exponent $n = 1$, the material is linear viscous and $n > 1$ denotes non-Newtonian viscosity, where viscosity increases under higher strain rates.

When plasticity is enabled, material deformation is dictated by the Mohr-Coulomb failure criterion:

$$\tau = C_0 - \sigma_n \tan \phi \tag{A5}$$

Solid Earth Discuss., https://doi.org/10.5194/se-2018-14
Manuscript under review for journal Solid Earth
Discussion started: 21 March 2018
© Author(s) 2018. CC BY 4.0 License.

where τ is the deviatoric shear stress, C_0 the material cohesion, σ_n the normal stress and ϕ the material angle of friction. For each model element, the effective stress τ_{eff} is calculated from strain rate:

$$\tau_{eff} = 2\mu\dot{\varepsilon}. \tag{A6}$$

If this effective stress exceeds the Mohr-Coulomb yield stress τ, elemental viscosity is reduced to an effective viscosity

$$\mu_{eff} = \frac{\tau}{2\dot{\varepsilon}}, \tag{A7}$$

otherwise viscosity is kept at the initial value.

Author contributions. Code development was done by M. Nettesheim with support of D. Whipp. M. Nettesheim designed and carried out simulations in close collaboration with T. Ehlers and D. Whipp. Finally, M. Nettesheim prepared the manuscript with contributions from all co-authors.

Competing interests. The authors declare that they have no competing interests.

Acknowledgements. This work was supported by a European Research Council (ERC) Consolidator Grant (615703) to T. Ehlers. We also acknowledge support by Deutsche Forschungsgemeinschaft and Open Access Publishing Fund of University of Tübingen. We thank J. Braun for providing the FastScape source code used for the coupled erosion-deformation simulations, and R. Bendick for thoughtful discussion over the years.

© Author(s) 2018. CC BY 4.0 License.

References

Bathe, K.-J.: Finite element procedures in engineering analysis, Prentice-Hall, New Jersey, 1982.

Bendick, R. and Ehlers, T. A.: Extreme localized exhumation at syntaxes initiated by subduction geometry, Geophysical Research Letters, 41, 2014GL061 026, https://doi.org/10.1002/2014GL061026, 2014.

Berger, A. L., Spotila, J. A., Chapman, J. B., Pavlis, T. L., Enkelmann, E., Ruppert, N. A., and Buscher, J. T.: Architecture, kinematics, and exhumation of a convergent orogenic wedge: A thermochronological investigation of tectonic–climatic interactions within the central St. Elias orogen, Alaska, Earth and Planetary Science Letters, 270, 13–24, https://doi.org/10.1016/j.epsl.2008.02.034, 2008.

Brandon, M. T., Roden-Tice, M. K., and Garver, J. I.: Late Cenozoic exhumation of the Cascadia accretionary wedge in the Olympic Mountains, northwest Washington State, Geological Society of America Bulletin, 110, 985–1009, https://doi.org/10.1130/0016-7606(1998)110<0985:LCEOTC>2.3.CO;2, 1998.

Braun, J.: Pecube: a new finite-element code to solve the 3D heat transport equation including the effects of a time-varying, finite amplitude surface topography, Computers & Geosciences, 29, 787–794, https://doi.org/10.1016/S0098-3004(03)00052-9, 2003.

Braun, J. and Willett, S. D.: A very efficient O(n), implicit and parallel method to solve the stream power equation governing fluvial incision and landscape evolution, Geomorphology, 180–181, 170–179, https://doi.org/10.1016/j.geomorph.2012.10.008, 2013.

Braun, J. and Yamato, P.: Structural evolution of a three-dimensional, finite-width crustal wedge, Tectonophysics, 484, 181–192, https://doi.org/10.1016/j.tecto.2009.08.032, 2010.

Braun, J., Thieulot, C., Fullsack, P., DeKool, M., Beaumont, C., and Huismans, R.: DOUAR: A new three-dimensional creeping flow numerical model for the solution of geological problems, Physics of the Earth and Planetary Interiors, 171, 76–91, https://doi.org/10.1016/j.pepi.2008.05.003, 2008.

Burg, J.-P., Nievergelt, P., Oberli, F., Seward, D., Davy, P., Maurin, J.-C., Diao, Z., and Meier, M.: The Namche Barwa syntaxis: evidence for exhumation related to compressional crustal folding, Journal of Asian Earth Sciences, 16, 239–252, https://doi.org/10.1016/S0743-9547(98)00002-6, 1998.

Capitanio, F. A., Morra, G., Goes, S., Weinberg, R. F., and Moresi, L.: India–Asia convergence driven by the subduction of the Greater Indian continent, Nature Geoscience, 3, 136, https://doi.org/10.1038/ngeo725, 2010.

Carter, N. L. and Tsenn, M. C.: Flow properties of continental lithosphere, Tectonophysics, 136, 27–63, https://doi.org/10.1016/0040-1951(87)90333-7, 1987.

Craw, D., Koons, P. O., Winslow, D. M., Chamberlain, C. P., and Zeitler, P. K.: Boiling fluids in a region of rapid uplift, Nanga Parbat Massif, Pakistan, Earth and Planetary Science Letters, 128, 169–182, https://doi.org/10.1016/0012-821X(94)90143-0, 1994.

Crowley, J. L., Waters, D. J., Searle, M. P., and Bowring, S. A.: Pleistocene melting and rapid exhumation of the Nanga Parbat massif, Pakistan: Age and P–T conditions of accessory mineral growth in migmatite and leucogranite, Earth and Planetary Science Letters, 288, 408–420, https://doi.org/10.1016/j.epsl.2009.09.044, 2009.

Dodson, M. H.: Closure temperature in cooling geochronological and petrological systems, Contributions to Mineralogy and Petrology, 40, 259–274, https://doi.org/10.1007/BF00373790, 1973.

Ehlers, T. A.: Computational Tools for Low-Temperature Thermochronometer Interpretation, Reviews in Mineralogy and Geochemistry, 58, 589–622, https://doi.org/10.2138/rmg.2005.58.22, 2005.

England, P. and Molnar, P.: Surface uplift, uplift of rocks, and exhumation of rocks, Geology, 18, 1173–1177, https://doi.org/10.1130/0091-7613(1990)018<1173:SUUORA>2.3.CO;2, 1990.

© Author(s) 2018. CC BY 4.0 License.

Enkelmann, E., Zeitler, P. K., Garver, J. I., Pavlis, T. L., and Hooks, B. P.: The thermochronological record of tectonic and surface process interaction at the Yakutat–North American collision zone in southeast Alaska, American Journal of Science, 310, 231–260, https://doi.org/10.2475/04.2010.01, 2010.

Enkelmann, E., Ehlers, T. A., Zeitler, P. K., and Hallet, B.: Denudation of the Namche Barwa antiform, eastern Himalaya, Earth and Planetary Science Letters, 307, 323–333, https://doi.org/10.1016/j.epsl.2011.05.004, 2011.

Enkelmann, E., Piestrzeniewicz, A., Falkowski, S., Stübner, K., and Ehlers, T. A.: Thermochronology in southeast Alaska and southwest Yukon: Implications for North American Plate response to terrane accretion, Earth and Planetary Science Letters, https://doi.org/10.1016/j.epsl.2016.10.032, 2016.

Falkowski, S., Enkelmann, E., and Ehlers, T. A.: Constraining the area of rapid and deep-seated exhumation at the St. Elias syntaxis, Southeast Alaska, with detrital zircon fission-track analysis, Tectonics, 33, 597–616, https://doi.org/10.1002/2013TC003408, 2014.

Finlayson, D. P., Montgomery, D. R., and Hallet, B.: Spatial coincidence of rapid inferred erosion with young metamorphic massifs in the Himalayas, Geology, 30, 219–222, https://doi.org/10.1130/0091-7613(2002)030<0219:SCORIE>2.0.CO;2, 2002.

Hayes, G. P., Wald, D. J., and Johnson, R. L.: Slab1.0: A three-dimensional model of global subduction zone geometries, Journal of Geophysical Research: Solid Earth, 117, B01 302, https://doi.org/10.1029/2011JB008524, 2012.

Heuret, A. and Lallemand, S.: Plate motions, slab dynamics and back-arc deformation, Physics of the Earth and Planetary Interiors, 149, 31–51, https://doi.org/10.1016/j.pepi.2004.08.022, 2005.

Hirth, G. and Kohlstedt, D.: Rheology of the upper mantle and the mantle wedge: A view from the experimentalists, in: Inside the subduction Factory, edited by Eiler, J., vol. 138 of *Geophysical Monograph Series*, pp. 83–105, American Geophysical Union, Washington, D. C., https://doi.org/10.1029/138GM06, 2003.

Jadamec, M. A. and Billen, M. I.: The role of rheology and slab shape on rapid mantle flow: Three-dimensional numerical models of the Alaska slab edge, Journal of Geophysical Research: Solid Earth, 117, B02 304, https://doi.org/10.1029/2011JB008563, 2012.

Koons, P. O., Zeitler, P. K., Chamberlain, C. P., Craw, D., and Meltzer, A. S.: Mechanical links between erosion and metamorphism in Nanga Parbat, Pakistan Himalaya, American Journal of Science, 302, 749–773, https://doi.org/10.2475/ajs.302.9.749, 2002.

Koons, P. O., Zeitler, P. K., and Hallet, B.: Tectonic Aneurysms and Mountain Building, in: Treatise on Geomorphology, edited by Owen, L. A. and Shroder, J. F., vol. 5 of *Reference Module in Earth Systems and Environmental Sciences*, pp. 318–349, Academic Press, San Diego, https://doi.org/10.1016/B978-0-12-374739-6.00094-4, 2013.

Lang, K. A., Huntington, K. W., Burmester, R., and Housen, B.: Rapid exhumation of the eastern Himalayan syntaxis since the late Miocene, Geological Society of America Bulletin, 128, 1403–1422, https://doi.org/10.1130/B31419.1, 2016.

Mahadevan, L., Bendick, R., and Liang, H.: Why subduction zones are curved, Tectonics, 29, TC6002, https://doi.org/10.1029/2010TC002720, 2010.

Malloy, M. A.: Rapid Erosion at the Tsangpo Knickpoint and Exhumation of Southeastern Tibet, Master's thesis, Lehigh Universiy, Bethlehem, Pennsylvania, 2004.

Molnar, P. and England, P.: Late Cenozoic uplift of mountain ranges and global climate change: chicken or egg?, Nature, 346, 29–34, https://doi.org/10.1038/346029a0, 1990.

Montgomery, D. R.: Valley incision and the uplift of mountain peaks, Journal of Geophysical Research: Solid Earth, 99, 13 913–13 921, https://doi.org/10.1029/94JB00122, 1994.

Reiners, P. W., Ehlers, T. A., and Zeitler, P. K.: Past, Present, and Future of Thermochronology, Reviews in Mineralogy and Geochemistry, 58, 1–18, https://doi.org/10.2138/rmg.2005.58.1, 2005.

© Author(s) 2018. CC BY 4.0 License.

Russo, R. M. and Silver, P. G.: Trench-Parallel Flow Beneath the Nazca Plate from Seismic Anisotropy, Science, 263, 1105–1111, https://doi.org/10.1126/science.263.5150.1105, 1994.

Schellart, W. P., Freeman, J., Stegman, D. R., Moresi, L., and May, D. A.: Evolution and diversity of subduction zones controlled by slab width, Nature, 446, 308–311, https://doi.org/10.1038/nature05615, 2007.

Schneider, D. A., Edwards, M. A., Kidd, W. S. F., Zeitler, P. K., and Coath, C. D.: Early Miocene anatexis identified in the western syntaxis, Pakistan Himalaya, Earth and Planetary Science Letters, 167, 121–129, https://doi.org/10.1016/S0012-821X(99)00022-9, 1999.

Simpson, G.: Role of river incision in enhancing deformation, Geology, 32, 341–344, https://doi.org/10.1130/G20190.2, 2004.

Stewart, R. J., Hallet, B., Zeitler, P. K., Malloy, M. A., Allen, Charlotte M., A., and Trippett, D.: Brahmaputra sediment flux dominated by highly localized rapid erosion from the easternmost Himalaya, Geology, 36, 711–714, https://doi.org/10.1130/G24890A.1, 2008.

Thieulot, C., Fullsack, P., and Braun, J.: Adaptive octree-based finite element analysis of two- and three-dimensional indentation problems, Journal of Geophysical Research: Solid Earth, 113, B12 207, https://doi.org/10.1029/2008JB005591, 2008.

Wang, P., Scherler, D., Liu-Zeng, J., Mey, J., Avouac, J.-P., Zhang, Y., and Shi, D.: Tectonic control of Yarlung Tsangpo Gorge revealed by a buried canyon in Southern Tibet, Science, 346, 978–981, https://doi.org/10.1126/science.1259041, 2014.

Whipp, D. M., Ehlers, Todd A., E., Braun, J., and Spath, C. D.: Effects of exhumation kinematics and topographic evolution on detrital thermochronometer data, Journal of Geophysical Research, 114, https://doi.org/10.1029/2008JF001195, 2009.

Whipp, D. M., Beaumont, C., and Braun, J.: Feeding the "aneurysm": Orogen-parallel mass transport into Nanga Parbat and the western Himalayan syntaxis, Journal of Geophysical Research: Solid Earth, 119, 5077–5096, https://doi.org/10.1002/2013JB010929, 2014.

Willett, S. D.: Orogeny and orography: The effects of erosion on the structure of mountain belts, Journal of Geophysical Research: Solid Earth, 104, 28 957–28 981, https://doi.org/10.1029/1999JB900248, 1999.

Willingshofer, E. and Sokoutis, D.: Decoupling along plate boundaries: Key variable controlling the mode of deformation and the geometry of collisional mountain belts, Geology, 37, 39–42, https://doi.org/10.1130/G25321A.1, 2009.

Winslow, D. M., Zeitler, P. K., Chamberlain, C. P., and Williams, I. S.: Geochronologic constraints on syntaxial development in the Nanga Parbat region, Pakistan, Tectonics, 15, 1292–1308, https://doi.org/10.1029/96TC00032, 1996.

Zeitler, P. K., Chamberlain, C. P., and Smith, H. A.: Synchronous anatexis, metamorphism, and rapid denudation at Nanga Parbat (Pakistan Himalaya), Geology, 21, 347–350, https://doi.org/10.1130/0091-7613(1993)021<0347:SAMARD>2.3.CO;2, 1993.

Zeitler, P. K., Meltzer, A. S., Koons, P. O., Craw, D., Hallet, B., Chamberlain, C. P., Kidd, W. S. F., Park, S. K., Seeber, L., and Bishop, M.: Erosion, Himalayan geodynamics, and the geomorphology of metamorphism, GSA Today, 11, 4–9, 2001.

Zeitler, P. K., Meltzer, A. S., Brown, L., Kidd, W. S., Lim, C., and Enkelmann, E.: Tectonics and topographic evolution of Namche Barwa and the easternmost Lhasa block, Tibet, in: Toward an Improved Understanding of Uplift Mechanisms and the Elevation History of the Tibetan Plateau, edited by Nie, J., Horton, B. K., and Hoke, G. D., vol. 507 of *GSA Special Papers*, Geological Society of America, https://doi.org/10.1130/2014.2507(02), 2014.